ARTICLE   OPEN

Solution-processed quantum-dot light-emitting diodes combining ultrahigh operational stability, shelf stability, and luminance

Zi Ye[1,2], Mengyu Chen[1,2], Xingtong Chen[1,2], Wenchen Ma[3], Xiaojuan Sun[1,2], Longjia Wu[4], Xiongfeng Lin[4], Yu Chen [ID][3 ✉] and Song Chen [ID][1,2 ✉]

The shelf-stability issue, originating from the ZnO-induced positive aging effect, poses a significant challenge to industrializing the display technology based on solution-processed quantum-dot light-emitting diodes (QLEDs). Currently, none of the proposed solutions can simultaneously inhibit exciton quenching caused by the ZnO-based electron-transporting layer (ETL) and retain other advantages of ZnO. Here in this work, we propose a bilayer design of ETL in which a buffer layer assembled of SnO_2 nanoparticles (NPs) suppresses the QD-ETL exciton quenching and tunes charge balance while ZnO NPs provide high electron conductivity. As a result, the bottom-emitting QLED combining capped ZnO and SnO_2 buffer exhibit a maximum luminance over 100,000 cd m^{-2} and a T_{95} operational lifetime averaging 6200 h at 1000 cd m^{-2} on the premise of entirely inhibiting positive aging.

INTRODUCTION

The display technology based on quantum-dot light-emitting diodes (QLEDs) features high display performance and low manufacturing costs[1–6]. Although the industrialization of the QLED is around the corner, the issues of device stability have not been entirely resolved. Apart from the underperforming operational stability of blue QLEDs, the shelf-stability issue caused by the so-called positive aging effect is another major challenge. It is unacceptable that high electroluminescence performance can only be achieved through an unpredictable period of shelf storage[7–11].

Several groups have studied the mechanism of positive aging in QLEDs. It was initially discovered that solution-processed ZnO nanoparticles (NPs) become electrically more conductive, and the photoluminescence (PL) of the emissive quantum dots is less quenched by the adjacent ZnO layer during the positive aging process[12]. Chen et al. tried to explain the above phenomenon from the perspective of oxygen vacancies[13]. Acharya et al. pointed out that the chemical reaction between ZnO and the encapsulation resin is the root cause[7]. According to a recent report by Zhang et al. surface stabilization in the form of HO-ZnO explains positive aging more generally[14]. However, isolating ZnO from ambient reactants does not solve the shelf-stability issue. Recent work shows that, although strict protection from moisture and other H$^+$ sources eliminates the surface reaction, the unstabilized ZnO surfaces lead to uncompetitive electroluminescence efficiencies and operational lifetimes[8].

One solution to realizing shelf-stable QLEDs without compromising other performance parameters is passivating the surfaces of ZnO NPs. Serval surface capping ligands have been attempted. Although various characterizations have proved that the ZnO surface can be partially passivated, successful demonstration at the device level is still missing[15]. The abundance of active surface sites and insufficient surface coverage may explain the

unsatisfactory results. Alternatively, shelf-stability can be achieved by blocking the exciton quenching channel between emissive QDs and the ZnO-based ETL during device fabrication if the electrical conductivity change of ZnO-based ETL occurs after a negligible period of shelf storage. Chen et al. observed that emissive QDs show negligible exciton quenching when deposited on ultrasmall ZnO NPs (<d> ~2.1 nm), and the design of a ZnO-based electron-transporting bilayer delivered QLEDs combining high operational stability and shelf stability[16]. However, small and insulating ZnO NPs limit the current density and maximum luminance. More recently, our group reported that an ETL based on SnO_2 NPs, known for their less active surface chemistry than ZnO, enabled QLEDs with shelf stability. This work also demonstrated ZnO-free QLED with a competitive operational lifetime[17]. However, the mobility of SnO_2 NPs still limits the maximum luminance. Therefore, to realize all the advantages of the ZnO ETL and eliminate positive aging, a combination of SnO_2 and ZnO is worth exploring.

Here in this work, based on the mechanisms of positive aging, we propose a bilayer design of ETL in which ZnO NPs are used to maintain high electron conduction, capping ligands reduce the surface chemistry activity of ZnO, a SnO_2 buffer inserted between emissive QDs and ZnO entirely suppresses the interface exciton quenching and tunes the balance of charge injection. With an optimized SnO_2–ZnO bilayer ETL, the bottom-emitting QLEDs with the conventional device structure show a maximum luminance over 100,000 cd m^{-2} and a T_{95} lifetime, defined as the time for luminescence to degrade to 95% of the initial value, as high as 6200 h under an initial luminance of 1000 cd m^{-2}. Our results demonstrate competitive QLED performances achieved on the premise of entirely inhibiting positive aging.

[1]Suzhou Key Laboratory of Novel Semiconductor-optoelectronics Materials and Devices, College of Chemistry, Chemical Engineering and Materials Science, Soochow University, Suzhou, Jiangsu, PR China. [2]Jiangsu Key Laboratory of Advanced Negative Carbon Technologies, Soochow University, Suzhou, Jiangsu, PR China. [3]School of Optoelectronic Science and Engineering & Collaborative Innovation Center of Suzhou Nano Science and Technology, Soochow University, Suzhou, Jiangsu, PR China. [4]TCL Corporate Research, Shenzhen, Guangdong, PR China. ✉email: chenyu_ny@suda.edu.cn; songchen@suda.edu.cn
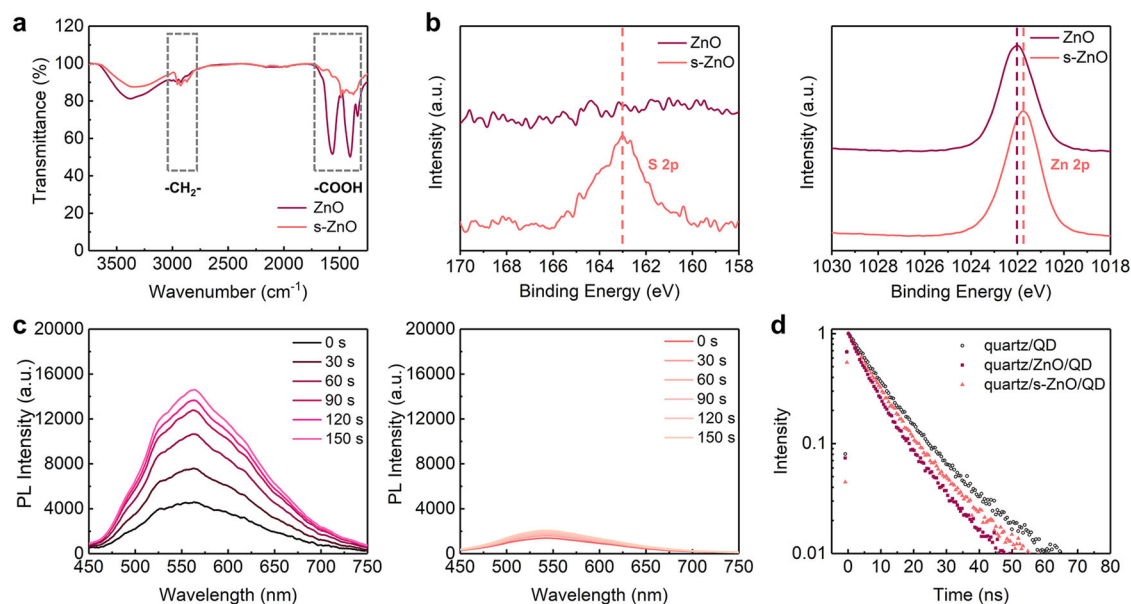
Fig. 1 ZnO nanoparticles with capping ligands. a FTIR of ZnO and s-ZnO. **b** S 2p (left) and Zn 2p (right) core-level XPS spectra. **c** Summary of t-PL of ZnO (left) and s-ZnO (right). **d** TRPL of QDs on quartz, QDs on ZnO/quartz, and QDs on s-ZnO/quartz.

RESULTS AND DISCUSSION

ZnO NPs with capping ligands

The unstabilized surface sites of ZnO NPs are the root cause of positive aging. To stabilize the ZnO surfaces, we choose to cap ZnO NPs with 3-mercapto-1-hexanol (MHL) through post-synthesis ligand exchange. To verify the effect of ligand exchange, we measure Fourier Transform Infrared (FTIR) spectroscopy, and the results are shown in Fig. 1a. The absorption peaks at 1566 and 1424 cm^{-1}, nearly absent in the spectrum for the s-ZnO NPs, are attributed to the carboxylate groups of pristine ligands. Moreover, prominent peaks at 2935 and 2856 cm^{-1} are assigned to the $-CH_2-$ stretching vibrations, confirming the addition of MHL onto the surfaces of ZnO NPs. Similar results have been reported when capping ZnO using 6-mercapto-1-hexanol[15]. Figure 1b shows the results of X-ray photoelectron spectroscopy (XPS). The emergence of S 2p (~163 eV) indicates the bonding between Zn and S upon the capping of MHL. The shift of Zn 2p, from 1022.0 to 1021.8 eV, confirms this conclusion as a Zn–S bond has lower binding energy than a Zn–O bond. As expected, the ligand exchange reaction does not change the average size and size distribution of ZnO NPs (see TEM images Supplementary Fig. 1).

Next, we verify the effect of surface stabilization by capturing the temporal PL of ZnO using a CCD-array spectrometer. The UV excitation starts once each sample is exposed to O_2 to evaluate the remaining adsorptive sites. As we have reported, under a continuous super-bandgap excitation, the chemical adsorption of oxygen occurs rapidly and results in significant growth of visible emission[14,18]. Therefore, the faster ramping of visible emission intensity, the higher number of remaining active surface sites. Figure 1c shows the visible emission monitored as a function of time. Supplementary Figure 2 shows the PL intensity plotted against time. The as-synthesized ZnO NPs show a rapid increase in visible emission, which remains low and stable for the s-ZnO NPs. The slow change of visible emission suggests a low number of adsorptive sites on the s-ZnO surface. However, the incomplete elimination of visible emission suggests low surface coverage of MHL. As reported by Gamelin's group, the capping group densities are still very low even when the visible emission is entirely suppressed by capping ZnO NPs with dodecylamine[19].

The results of time-resolved photoluminescence (TRPL) further confirm the above conclusion. Figure 1d compares the PL decay

curves measured from CdSe/Cd$_{1-x}$Zn$_x$Se/ZnSe QDs deposited on three different substrates. All the decay curves can be decently fitted using biexponential functions (see fitting parameters in Supplementary Table 1). The fast components (τ_1) vary significantly across all these samples, while the slow components (τ_2) are similar. Although the capping of MHL increases τ_1 from 5.2 to 6.98 ns, the quenching effect is still apparent ($\tau_1 = 8.29$ ns for QD/quartz). Therefore, we speculate that low surface coverage of capping ligands on ZnO NPs limits the enhancement of shelf stability.

The SnO$_2$ buffer layer

Since ligand exchange cannot fully stabilize the surface ZnO NPs, additional strategies should be considered. The mechanism of positive aging reveals that blocking the charge transfer channels between emissive QDs and ZnO can improve shelf stability without compromising electroluminescence performances. The buffer layer used here is assembled of SnO$_2$ NPs, an n-type ETL material with similar electronic levels but less surface activity. Notably, the function of SnO$_2$ proposed here significantly differs from previous reports[17,20]. Through the post-treatment in tetramethylammonium hydroxide (TMAH) solution, NPs can decently disperse in ethanol (see TEM images in Supplementary Fig. 3)[17], which is compatible with the fabrication process of the conventional structure.

Ultraviolet photoelectron spectroscopy (UPS) measurement is carried out to profile the alignment of electronic levels across the QD/SnO$_2$/ZnO multilayered stack. Although a complete depth profile is not achievable due to the solution process, the energy-level alignment acquired by sequential deposition and measurement is more informative than that based on isolated materials. Figure 2a shows the cutoff and valance signals. Figure 2b shows the optical bandgaps. As summarized in Fig. 2c, the CdSe/Cd$_{1-x}$Zn$_x$Se/ZnSe QDs deposited on ITO/PEDOT:PSS/TFB substrate show a Fermi level of 4.10 eV below its vacuum level and a HOMO level of −5.6 eV. After depositing TMAH-SnO$_2$ NPs on QDs, the Fermi and HOMO levels shift to −3.9 and −7.52 eV, respectively. After further depositing ZnO on top of SnO$_2$, the Fermi level and HOMO level shift to −3.96 and −7.3 eV, respectively. Fermi-level alignment causes a downward vacuum-level shift at the QD-SnO$_2$ interface and an upward vacuum-level shift at the SnO$_2$-ZnO
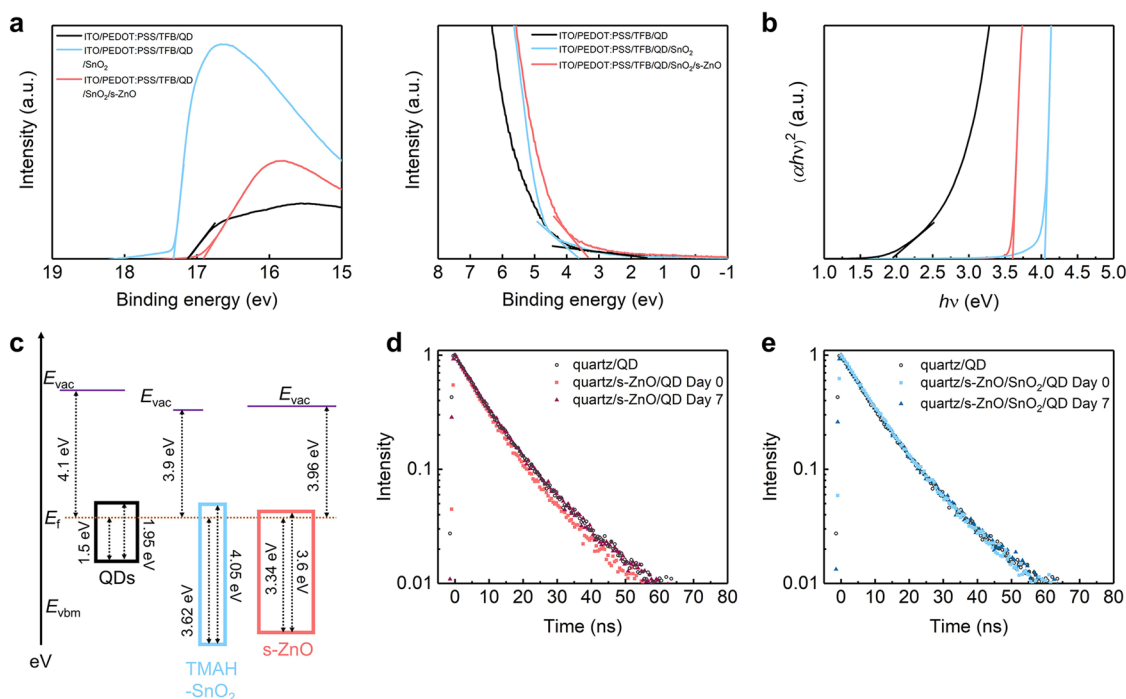
Fig. 2 SnO₂ buffer layer. a Cutoff (left) and valance (right) spectra of ITO/PEDOT:PSS/TFB/QD, ITO/PEDOT:PSS/TFB/QD/SnO₂, ITO/PEDOT:PSS/TFB/QD/SnO₂/s-ZnO. **b** The optical bandgap of the QD, SnO₂, and s-ZnO films. **c** The energy-level alignment of a QD/SnO₂/s-ZnO stack which is deposited on an ITO/PEDOT:PSS/TFB substrate. **d** TRPL of QDs on quartz, QDs on s-ZnO/quartz at Day 0 and Day 7. **e** TRPL of QD on quartz, QD on s-ZnO/SnO₂/quartz at Day 0 and Day 7.

interface. The energy-level profile shown in Fig. 2c is supposed to provide efficient electron injection, and the thickness of the SnO₂ layer serves as a knob to adjust the charge balance.

Besides the requirement of electronic levels, the inserted SnO₂ layer is expected to protect the emissive QDs from ZnO-induced exciton quenching. To verify this, we conduct TRPL measurements for CdSe/Cd$_{1-x}$Zn$_x$Se/ZnSe QDs deposited on variant substrates. Again, the main difference in the decay curves of each sample comes from τ_1. Figure 2d shows that the QDs show τ_1 of 6.98 ns when deposited on s-ZnO substrates. After being shelf-stored for seven days in air ambient, τ_1 increases slightly to 8.14 ns, which almost matches QD/quartz ($\tau_1 = 8.29$ ns). For the QD/SnO₂/s-ZnO sample, as shown in Fig. 2e, τ_1 reaches 8.08 ns even without shelf storage and remains stable after seven days. Therefore, the buffer layer assembled of SnO₂ NPs successfully stabilizes the QDs' PL decay kinetics. The mechanism for reducing the exciton quenching rate is ascribed to the reduction of the photoinduced electron-transfer rate and the lower number of charge acceptors on SnO₂ surfaces[17].

The exciton quenching across the QD-oxide type-II heterojunction is dominated by photoinduced or defect-related electron transfer from emissive QDs to ETL, which has been extensively studied for photovoltaics and related solar-harvesting devices[6,21,22]. Also, reports indicate holes could be transferred from QDs to ETL[13,16]. In our view, although the deep donor levels of V$_O$ are available for capturing holes when the Fermi level of ZnO approaches the conduction band minimum (CBM)[23,24], the subsequent recombination between the captured hole and a CBM electron has never been reported. The transferred holes in QDs can also be scavenged by solvent residuals like ethanol[25,26]. However, this would be inconsistent with our TRPL results. Given that SnO₂ NPs are dispersed and processed using ethanol (Fig. 2e), the TRPL of the QD/SnO₂/s-ZnO sample proves negligible hole transfer.

QLED with a SnO₂-ZnO bilayer ETL

Based on the above results, SnO₂ is a promising buffer material for the conventional QLED structure, shown in Fig. 3a. Figure 3b summarizes the L-J-V curves of QLED devices with fully aged s-ZnO and SnO₂/s-ZnO as ETLs, respectively. Figure 3c shows the EL spectra. Figure 3d summarizes the electroluminescence efficiencies. The comparison of the two sets of curves leads to the following conclusions. First, adding the SnO₂ buffer layer does not significantly reduce electron injection. The device exhibits a similar threshold turn-on (V_{th}) compared with the s-ZnO-based counterpart and a significantly higher maximum luminance (approaching 200,000 cd m^{-2}) than any previously reported shelf-stable QLED[16,17]. Second, the SnO₂ buffer layer suppresses the leakage current, mainly from hole leakage through ETL[27]. Third, tuning the thickness of the SnO₂ layer is critical for charge balance. With an optimized thickness of the SnO₂ layer (~12 nm), the EQE and current efficiency reach their maximum values at a bias as low as 2.3 V (see data for other SnO₂ thicknesses in Supplementary Fig. 4). The device optimization mentioned above prioritizes operational lifetime, which is discussed in the following. Besides, QLEDs with fully aged SnO₂/ZnO (or ZnO) show slightly inferior performance than the SnO₂/s-ZnO (or s-ZnO) counterparts, indicating the positive effect of MHL capping (see data in Supplementary Figs. 5, 6).

The operational lifetimes are measured under constant current density. Figure 3e shows the luminance of a fully aged s-ZnO-based QLED decays from 23,100 to 22,000 cd m^{-2} after 20.4 h. With an acceleration factor of 1.80 (see Supplementary Fig. 7), that result corresponds to a T_{95} averaging 5800 h at 1000 cd m^{-2}. Meanwhile, a fully aged ZnO-based device shows a similar T_{95} lifetime of 5600 h. However, it is worth mentioning that shelf storage is required for the s-ZnO- or ZnO-based QLED to achieve such high lifetimes. For example, a freshly-made ZnO-based QLED shows a T_{95} of only 2500 h. The above comparisons confirm that the underpinning mechanism of positive aging is the surface stabilization of ZnO. A SnO₂ buffer is introduced to eliminate

positive aging without compromising other device performances. Figure 3e also shows the lifetime results of QLED with a SnO$_2$/s-ZnO bilayer ETL. The device without shelf storage shows an average (/ champion) T_{95} as high as 6200 h (/7200 h) at 1000 cd m^{-2} with decent reproducibility, translating to a T_{95} of 390,000 h (/450,000 h) at 100 cd m^{-2}. Digital images show uniform emission across the pixel after the lifetime test, which avoids overestimating the operational lifetime[28]. QLEDs with SnO$_2$/ZnO as ETL show a slightly lower T_{95} lifetime averaging 6000 h. In addition to Fig. 3e, the operation lifetime data mentioned above are summarized in Supplementary Figs. 8–10.
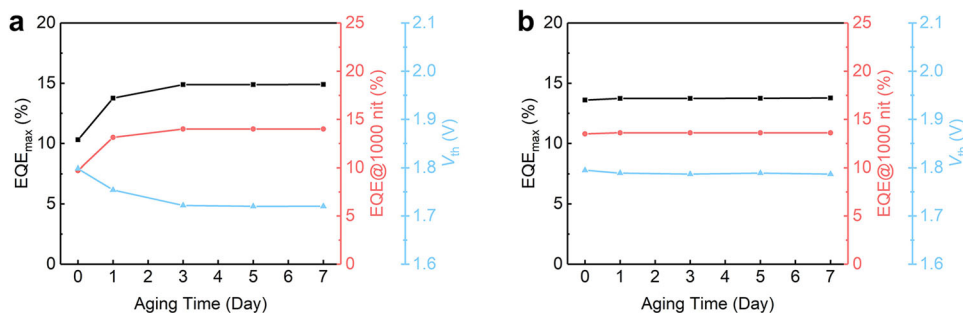
Shelf stability

Operational stability and shelf stability must be combined in the same device. The motivation for employing the SnO$_2$/s-ZnO bilayer QLED is to solve the shelf-stability issue. To compare the shelf stability of QLEDs based on different ETLs, we monitored V_{th}, EQE$_{max}$, and EQE@1000 cd m^{-2} as a function of shelf-storage time. The results are summarized in Fig. 4, and additional data can be found in Supplementary Figs. 11–13. The performance of an s-ZnO-based device changes significantly as a function of shelf-storage time. EQE$_{max}$ increases from 10.3% (fresh) to 14.9% (at day

7), while V_{th} reduces from 1.8 V to 1.7 V. In contrast, all the parameters measured from the bilayer-ETL-based device remain reasonably stable over the testing period. The images of the emitting pixels indicate that adding the SnO$_2$ buffer prevents the development of dark spots during shelf storage. The L-J-V curves of these devices are almost storage-time independent, suggesting ultrastable electronic properties at the device level. In particular, the exciton quenching caused by unstabilized ZnO is effectively suppressed by adding SnO$_2$, resulting in entirely suppressed positive aging and shelf stability. Combining the T_{95} of 6200 h, luminance over 100,000 cd m^{-2}, and shelf stability, our QLEDs demonstrate overall competitive performances compared to other benchmarking devices (see Supplementary Table 2).

Two additional characterizations further confirm the effectiveness of the SnO$_2$ buffer at the device level. First, the ETL-induced exciton quenching can affect the alignment of energy levels, and so is the flat-band voltage of the emissive layer (V_{FB_EML}). The value of V_{FB_EML} is obtained by fitting the bias-dependent electro-absorption (EA) signal of the QDs. The intensity of the signal measures the internal electric field intensity of the QD layer, as we have detailed in the previous reports[14,27,29]. Therefore, the bias at which the internal electric intensity becomes zero is the V_{FB_EML}.
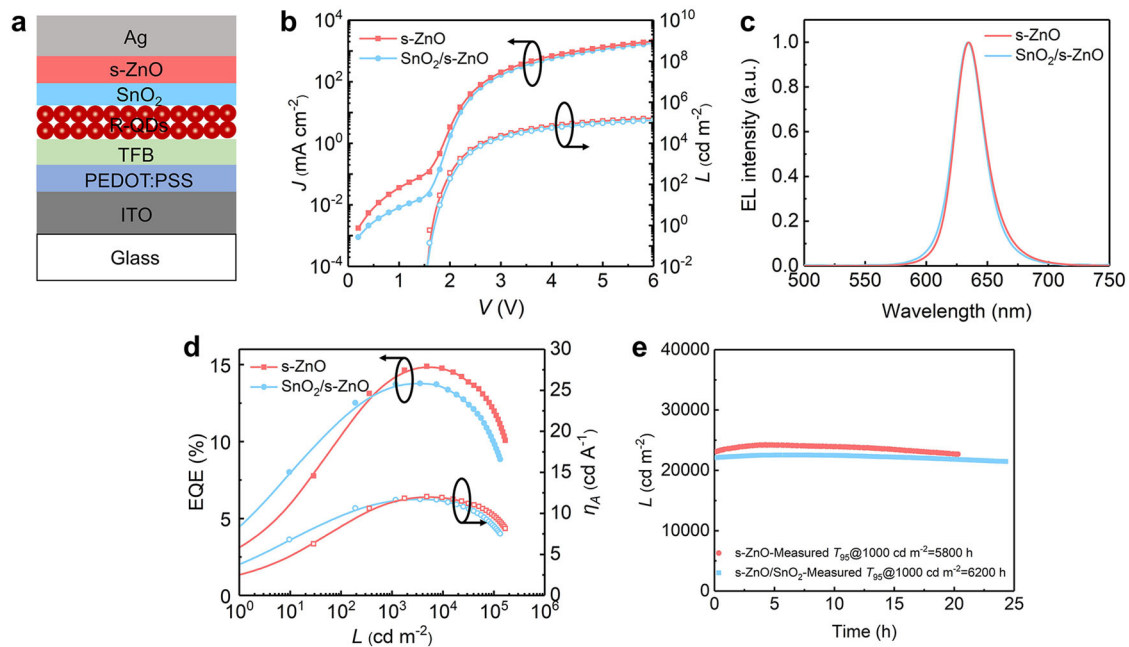
Fig. 3 QLED with a SnO$_2$-ZnO bilayer ETL. a Device structure. **b** L-J-V of QLEDs with s-ZnO or SnO$_2$/s-ZnO as ETL. **c** EL spectra of QLEDs with s-ZnO or SnO$_2$/s-ZnO as ETL. **d** EQE and current efficiency of QLEDs with s-ZnO or SnO$_2$/s-ZnO as ETL. **e** Operational lifetime tests of QLEDs with s-ZnO or SnO$_2$/s-ZnO as ETL (under a constant current density of 170 mA cm^{-2}). The s-ZnO-based QLEDs were tested after being shelf-stored for 20 days.

Fig. 4 Shelf stability. EQE$_{max}$, EQE@1000 cd m^{-2}, V_{th}, of QLEDs (**a**) with s-ZnO or (**b**) SnO$_2$/s-ZnO as ETL. The results are monitored as a function of shelf-storage time.
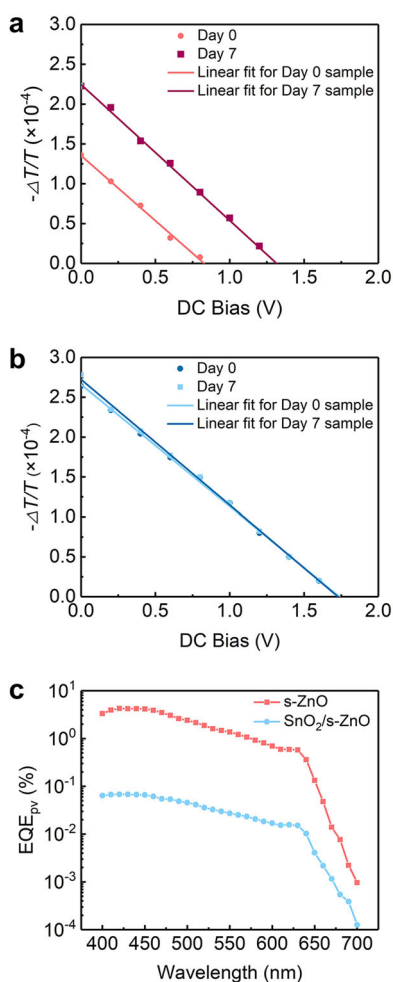
Fig. 5 Interfacial charge transfer. Bias-dependent electro-absorption for QLED with (**a**) s-ZnO or (**b**) SnO_2/s-ZnO as ETL. The probing wavelength is set at 630 nm. **c** EQE_{PV} for QLEDs with s-ZnO or SnO_2/s-ZnO as ETL.

As seen in Fig. 5a, the s-ZnO-based device experiences a significant increase of V_{FB_EML} (from 0.8 to 1.3 V) after being shelf-stored for seven days, indicating that the gradually stabilized ZnO surface results in an upward shift of Fermi levels in the ETL. The change was correlated with reduced exciton quenching and the lifted quasi-Fermi level of electrons[14]. Notably, one may argue that the increase of V_{FB_EML} is seemingly inconsistent with the reduction of V_{th} shown in Fig. 4a. In fact, for a non-fully aged ZnO-based QLED, the low V_{FB_EML} suggested by EA does not necessarily translate to a low V_{th}. A significant electron injection barrier and unsaturated electron conductivity could result in substantial voltage consumption. Figure 5b shows the EA results of the device with a bilayer ETL. Due to the suppressed exciton quenching, the quasi-Fermi level of electrons is effectively stabilized by adding a SnO_2 buffer, resulting in a highly stable energy-level alignment across the QD-ETL heterojunction ($V_{FB\_EML} = 1.7$ V).

According to the TRPL results, we conclude that the ZnO-induced exciton quenching occurs through the photoinduced electron transfer and other interfacial charge transfers involving ETL's surface localized states. To independently confirm the first mechanism, we operate QLED devices under the photovoltaic mode and measure their EQE_{PV} spectra. It is well recognized that the photovoltaic effect of QD-oxide heterojunction is collectively determined by the efficiencies of photon absorption, exciton dissociation, and charge extraction, in which exciton dissociation is described using photoinduced electron transfer from emissive

QDs to the oxide ETL[30,31]. In Fig. 5c, the photovoltaic response of $\lambda \leq 620$ nm comes from the first excitonic and super-bandgap excitations of QDs, while the sub-bandgap signal is ascribed to the transitions involving surface localized states. Comparing the two spectra, we find that adding the SnO_2 reduces the EQE_{PV} values at the super-bandgap region by almost two orders of magnitude. The two devices are supposed to absorb similar photon flux and experience similar extraction loss due to the very similar device structure. Therefore, the significant gap of EQE_{PV} in the super-bandgap region is consistent with our conclusion that adding SnO_2 buffer suppresses the photoinduced electron transfer from QD to ETL. According to the many-state Marcus model, the photoinduced charge transfer rate increases substantially with the system's free energy change ($-\Delta G$). Among various sources of $-\Delta G$, the CBM offset across the donor-acceptor interface has been considered a primary factor[32,33]. Therefore, the significant reduction of exciton quenching by adding SnO_2 (see Fig. 2c) can be partially ascribed to the small CBM offset between QDs and SnO_2 NPs. In addition, the lower number of active sites on SnO_2 surfaces is also an essential factor. Interestingly, the reduction of EQE_{PV} in the sub-bandgap region is only about ten times, indicating that the electron-transfer rate is limited by the energetically-upward hopping from the localized surface states to relatively delocalized states within QDs.

In conclusion, we demonstrate a method to realize shelf-stable QLED while maintaining operational lifetimes and high luminance. To stabilize the ZnO surface, we cap ZnO NPs using MHL. Given the incomplete surface coverage, we employ a buffer layer based on TMAH-capped SnO_2 NPs to suppress the ZnO-induced exciton quenching without compromising electron conduction. PL studies prove that such a combination can successfully suppress the interface electron transfer, resulting in shelf stability. EA and EQE under photovoltaic mode confirm the conclusion at the device level. As a result, our SnO_2/s-ZnO-based QLED demonstrates a maximum luminance exceeding 100,000 cd m^{-2}, a T_{95}@1000 cd m^{-2} of 6200 h, and a T_{95}@100 cd m^{-2} of 390,000 h on the premise of inhibiting positive aging.

METHODS

Materials synthesis

For a typical synthesis of ZnO nanoparticles, a solution of zinc acetate dihydrate ($ZnAc_2\cdot 2H_2O$) (3 mmol) dissolved in dimethyl sulfoxide (DMSO) (30 mL) is added dropwise to a solution of tetramethylammonium hydroxide (TMAH) (6.5 mmol) dissolved in ethanol (30 mL), followed by stirring for 1 h in ambient air. The resulting ZnO NPs were washed and dispersed in ethanol. For capping 3-mercapto-1-hexanol (MHL) onto the surface of ZnO NPs, a mixture of MHL (0.5 mmol) and TMAH (0.4 mmol) dissolved in 1 mL of ethanol was mixed with the above ZnO NPs solution and then stirred for 30 min in ambient air. The resulting s-ZnO NPs solution was washed and dispersed in ethanol for device fabrication.

TMAH-SnO_2 NPs were synthesized according to the method reported previously by our group[17]. The resulting TMAH-SnO_2 NPs were dispersed in ethanol for device fabrication.

The red quantum dots used in this work were synthesized based on the recipe reported in the literature with appropriate modifications[34]. For a typical synthesis of $CdSe/Cd_{1-x}Zn_xSe/ZnSe$ QDs, CdO (0.4 mmol), $ZnAc_2\cdot 2H_2O$ (6 mmol), and oleic acid (OA) were mixed and then heated to 170 °C in flowing high-purity argon for 30 min. Then 15 mL of 1-octadecene (ODE) was introduced, and the temperature was elevated to 300 °C. A solution containing 0.9 mmol of selenium (Se) dissolved in 2 mL of trioctylphosphine (TOP) was quickly injected into the reaction system, and the reaction temperature was kept for 10 min. After that, 0.1 mmol Se dissolved in 1 mL TOP was injected at the elevated temperature of 300 °C and reacted for another 10 min. Finally, the reaction mixture

was cooled to room temperature, followed by washing and dispersing in octane for device fabrication.

All the chemicals and organic solvents were purchased from Sigma-Aldrich. The resulting NPs solution was filtered (0.22 μm PTFE filter) before use.

Materials characterizations

The transmission electron microscope (TEM) was carried out with an FEI TECNAI G20 (with an acceleration voltage of 200 kV). Fourier transform infrared spectra measurements were performed by a Bruker Tensor 27 on solid-state samples. XPS measurements were carried out with an X-ray photoelectron spectrometer (Thermo Fisher Scientific ESCALAB 250 Xi). The t-PL of ZnO and s-ZnO films were obtained using a spectral CCD-array spectrometer (Ocean Optics USB2000) and a laser source (CNI laser UV-F-320, 10 mW at 320 nm). Samples were housed in a cryostat which is connected to a vacuum pump (based pressure ~10^{-3} Torr) and O_2 source. The integration time of the spectrometer was fixed at 1000 ms. The time-resolved PL (TRPL) decay transients were recorded by an FLS1000 (Edinburgh Instrument). All film samples were annealed at 80 °C during all of the above characterization tests. Ultraviolet photoelectron spectroscopy (UPS) was measured with Escalab 250Xi (Thermo Fisher Scientific) ultrahigh vacuum surface analysis system equipped with a He-discharge lamp providing He-I photons of 21.22 eV. The samples were prepared and transferred to the measurement setup without exposure to air. The absorption spectra were measured by a UV3600 (Shimadzu).

Device fabrication

The patterned ITO substrates were sequentially cleaned in an ultrasonic bath of glass cleaner, deionized water, acetone, and isopropanol for 10 min each, followed by drying with N_2 and cleaning by UV-ozone for 15 min before device fabrication. The PEDOT: PSS solution was spin-casted onto ITO-coated glass substrates at 5500 rpm for 45 s and then baked at 150 °C for 15 min. The TFB solution (8 mg mL^{-1}) was on PEDOT: PSS at 3000 rpm for 30 s and was baked at 150 °C for 30 min. The QDs were deposited on the top of the ITO/PEDOT: PSS/TFB stack by spin-coating at 1000 rpm for 40 s. Then the TMAH-SnO$_2$ NPs (10 mg mL^{-1}) and the s-ZnO nanoparticles (30 mg mL^{-1}) were layer-by-layer deposited onto the QDs layer. The TMAH-SnO$_2$ and s-ZnO layers were baked at 80 °C for 30 min. Finally, 100 nm Ag was thermally evaporated under a high vacuum (4×10^{-4} Pa) at a deposition rate of 0.6 Å s^{-1}. UV-curable resins (LOCTITE 3335) were used to encapsulate the devices by covering glass slides in a glovebox. Each pixel has an active area of 4 mm^2.

Device characterizations

The L-J-V characteristics of the devices were measured by a programmed system comprising a source meter (Keithley 2400) for J(V), a calibrated silicon detector (Edmund) coupled with a Keithley 6485 picoammeter for the collection of photons, and a CCD-array spectrometer (Ocean Optics FLAME-T-VIS-NIR-ES) for spectra and the calculation of L(V). EQE$_{PV}$ spectra were measured with a system composing a 500 W Xe light source (Zolix X500A), a monochromator (Newport CS260), an optical chopper, calibrated photo-detectors (Thorlabs DET100A2), a low-noise current pre-amplifier (SR570, amplification ratio = 10^6) and a lock-in amplifier (SR830, time constant = 0.3 s). The devices were measured without applying an external bias. For the electro-absorption (EA) measurements, a monochromatic beam probes the sample through the ITO side, and the change of optical absorption is detected in the reflection mode. The signal is further processed through a current amplifier and a lock-in amplifier. The final signal is the ratio of signals with and without AC field modulation. In the measurements of built-in potential, the probing wavelength is fixed at the first exciton transition of the QDs, and the DC bias was scanned. The operational lifetime test was conducted under ambient conditions. The sample was electrically driven by a Keithley 2400 source-measure unit, which also measured the bias through the device. The emission from the device was detected with a calibrated silicon detector (Edmund) coupled with a Keithley 6485 picoammeter. For the test of T_{95} operational lifetimes, the encapsulated samples were measured under ambient conditions using a commercialized lifetime test system (Guangzhou New Vision Opto-electronic Technology Co. Ltd.).

REFERENCES

1. Shirasaki, Y., Supran, G. J., Bawendi, M. G. & Bulović, V. Emergence of colloidal quantum-dot light-emitting technologies. *Nat. Photonics* **7**, 13–23 (2012).
2. Dai, X., Deng, Y., Peng, X. & Jin, Y. Quantum-dot light-emitting diodes for large-area displays: towards the dawn of commercialization. *Adv. Mater.* **29**, 1607022 (2017).
3. Sun, Y., Jiang, Y., Sun, X. W., Zhang, S. & Chen, S. Beyond OLED: Efficient quantum dot light-emitting diodes for display and lighting application. *Chem. Rec.* **19**, 1729–1752 (2019).
4. Vasilopoulou, M. et al. Advances in solution-processed near-infrared light-emitting diodes. *Nat. Photonics* **15**, 656–669 (2021).
5. Ren, A. et al. Emerging light-emitting diodes for next-generation data communications. *Nat. Electron.* **4**, 559–572 (2021).
6. Liu, M. et al. Colloidal quantum dot electronics. *Nat. Electron.* **4**, 548–558 (2021).
7. Acharya, K. P. et al. High efficiency quantum dot light emitting diodes from positive aging. *Nanoscale* **9**, 14451–14457 (2017).
8. Chen, Z., Su, Q., Qin, Z. & Chen, S. Effect and mechanism of encapsulation on aging characteristics of quantum-dot light-emitting diodes. *Nano Res.* **14**, 320–327 (2021).
9. Ding, S. et al. Impact of the resistive switching effects in ZnMgO electron transport layer on the aging characteristics of quantum dot light-emitting diodes. *Appl. Phys. Lett.* **117**, 093501 (2020).
10. Su, Q., Zhang, H., Sun, Y., Sun, X. W. & Chen, S. Enhancing the performance of quantum-dot light-emitting diodes by postmetallization annealing. *ACS Appl. Mater. Interfaces* **10**, 23218–23224 (2018).
11. Lin, B.-Y. et al. Performance improvement of blue quantum dot light-emitting diodes by facilitating electron transportation and suppressing electroplex emission. *Chem. Eng. J.* **417**, 127983 (2021).
12. Ding, W.-C. et al. Positive aging mechanisms for high-efficiency blue quantum dot light-emitting diodes. *Dig. Tech. Pap. Soc. Inf. Disp. Int. Symp.* **49**, 1622–1624 (2018).
13. Su, Q., Sun, Y., Zhang, H. & Chen, S. Origin of positive aging in quantum-dot light-emitting diodes. *Adv. Sci.* **5**, 1800549 (2018).
14. Zhang, W. et al. Positive aging effect of ZnO nanoparticles induced by surface stabilization. *J. Phys. Chem. Lett.* **11**, 5863–5870 (2020).
15. Chen, D. et al. Thiol modification enables ZnO-nanocrystal films with atmosphere-independent conductance. *J. Phys. Chem. C* **125**, 20022–20027 (2021).
16. Chen, D. et al. Shelf-stable quantum-dot light-emitting diodes with high operational performance. *Adv. Mater.* **32**, e2006178 (2020).
17. Chen, M. et al. Highly stable SnO2-based quantum-dot light-emitting diodes with the conventional device structure. *ACS Nano* **16**, 9631–9639 (2022).
18. Ma, Y. et al. Charge transfer-induced photoluminescence in ZnO nanoparticles. *Nanoscale* **11**, 8736–8743 (2019).
19. Norberg, N. S. & Gamelin, D. R. Influence of surface modification on the luminescence of colloidal ZnO nanocrystals. *J. Phys. Chem. B* **109**, 20810–20816 (2005).
20. Chen, Z. & Chen, S. Efficient and stable quantum-dot light-emitting diodes enabled by tin oxide multifunctional electron transport layer. *Adv. Opt. Mater.* **10**, 2102404 (2022).
21. Bang, J. H. & Kamat, P. V. Quantum dot sensitized solar cells. A tale of two semiconductor nanocrystals: CdSe and CdTe. *ACS Nano* **3**, 1467–1476 (2009).

22. Chen, H. M. et al. Quantum dot monolayer sensitized ZnO nanowire-array photoelectrodes: true efficiency for water splitting. *Angew. Chem. Int. Ed.* **49**, 5966–5969 (2010).
23. Zhang, S. B., Wei, S. H. & Zunger, A. Intrinsicn-type versusp-type doping asymmetry and the defect physics of ZnO. *Phys. Rev. B* **63**, 075205 (2001).
24. Vidya, R. et al. Energetics of intrinsic defects and their complexes in ZnO investigated by density functional calculations. *Phys. Rev. B* **83**, 045206 (2011).
25. Van Dijken, A., Meulenkamp, E. A., Vanmaekelbergh, D. & Meijerink, A. Influence of adsorbed oxygen on the emission properties of nanocrystalline ZnO particles. *J. Phys. Chem. B* **104**, 4355–4360 (2000).
26. Cohn, A. W., Janßen, N., Mayer, J. M. & Gamelin, D. R. Photocharging ZnO nanocrystals: picosecond hole capture, electron accumulation, and auger recombination. *J. Phys. Chem. C.* **116**, 20633–20642 (2012).
27. Luo, H. et al. Origin of subthreshold turn-on in quantum-dot light-emitting diodes. *ACS Nano* **13**, 8229–8236 (2019).
28. Jin, W. et al. On the accurate characterization of quantum-dot light-emitting diodes for display applications. *npj Flex. Electron.* **6**, 35 (2022).
29. Chen, S. et al. On the degradation mechanisms of quantum-dot light-emitting diodes. *Nat. Commun.* **10**, 765 (2019).
30. Lan, X., Masala, S. & Sargent, E. H. Charge-extraction strategies for colloidal quantum dot photovoltaics. *Nat. Mater.* **13**, 233–240 (2014).
31. Žídek, K., Zheng, K., Chábera, P., Abdellah, M. & Pullerits, T. Quantum dot photodegradation due to CdSe-ZnO charge transfer: Transient absorption study. *Appl. Phys. Lett.* **100**, 243111 (2012).
32. Tvrdy, K., Frantsuzov, P. A. & Kamat, P. V. Photoinduced electron transfer from semiconductor quantum dots to metal oxide nanoparticles. *Proc. Natl Acad. Sci. U.S.A.* **108**, 29–34 (2011).
33. Tisdale, W. A. et al. Hot-electron transfer from semiconductor nanocrystals. *Science* **328**, 1543–1547 (2010).
34. Cao, W. et al. Highly stable QLEDs with improved hole injection via quantum dot structure tailoring. *Nat. Commun.* **9**, 2608 (2018).

AUTHOR CONTRIBUTIONS
Z.Y. contributed to the fabrication and characterizations of devices. Z.Y., M.C. and W.M. contributed to the synthesis and characterizations of SnO_2 NPs and ZnO NPs. X.C. contributed to the study of electro-absorption and EQE_{PV}. X.S. assisted with device fabrication. L.W. and X.L. contributed to the synthesis of quantum dots. S.C. and Y.C. conceived the idea and supervised the experiments. The paper was written through contributions of all authors. All authors have given approval to the final version of the paper.

COMPETING INTERESTS
The authors declare no competing interests.

ADDITIONAL INFORMATION
Supplementary information The online version contains supplementary material available at https://doi.org/10.1038/s41528-022-00231-2.

Correspondence and requests for materials should be addressed to Yu Chen or Song Chen.

Reprints and permission information is available at http://www.nature.com/reprints

Publisher's note Springer Nature remains neutral with regard to jurisdictional claims in published maps and institutional affiliations.